Journal of the Optical Society of America B
OPTICAL PHYSICS

Multifunctional plasmonic metasurface demultiplexer and wavelength-polarization controllable beam splitter

MARIA I. BENETOU[1,*] AND KOSMAS L. TSAKMAKIDIS[2,3]

[1]Mbh-Qet. Ltd, Kemp House, 160 City Road, EC1V 2NX, London, UK
[2]Section of Condensed Matter Physics, Department of Physics, National and Kapodistrian University of Athens, Panepistimioupolis, GR-157 84 Athens, Greece
[3]e-mail: ktsakmakidis@phys.uoa.gr
*Corresponding author: mbenetou@mbhqet.com

Received 1 April 2021; revised 8 June 2021; accepted 17 June 2021; posted 18 June 2021 (Doc. ID 426434); published 14 July 2021

We report the experimental realization of a multifunctional microscale plasmonic metasurface capable of sampling a light beam and performing five functionalities, while allowing high direct transmission and maintenance of the properties of the input light beam. The plasmonic metasurface integrates light-to-surface-plasmon coupling, two-channel wavelength demultiplexing with a channel spacing smaller than 44 nm, wavelength and polarization controllable beam splitting of a *monochromatic, single polarization* signal, and four-level polarization and wavelength-polarization demultiplexing in an all-in-one structure. Such a device can play a key role for on-chip adaptable integrated circuits for parallel signal processing, communications, and nondestructive sensing.

https://doi.org/10.1364/JOSAB.426434

1. INTRODUCTION

Plasmonics exploiting surface plasmons, the collective oscillations of free electrons on a metal–dielectric interface, can break the diffraction limit and couple light into intense, engineered, localized deep-subwavelength guided modes [1,2]. Combining the size of nanoelectronics with the speed and high bandwidth of dielectric photonics, they can enable devices that can naturally interact with both technologies allowing for powerful, ultracompact, on-chip photonic circuits for rapid data transmission and signal processing [1]. The use of multiplexing technologies, such as wavelength, polarization, or the combined wavelength-polarization multiplexing to increase even further the bandwidth of a communication link is already well established [3–15]. In such multiplexing techniques, the information is encoded at different conditions, viz., different operating wavelengths, polarization states, or wavelength-polarization conditions [3–17]. The information density of the link is multiplied by the number of the multiplexed conditions, each of the conditions carries a different signal, and all of them simultaneously propagate over a waveguide [3–17]. At the receiver end of such communication links, a *demultiplexer* separates those conditions and routes the information encoded in them to uniquely related directions. In this concept, ultracompact, microscale demultiplexers capable of offering a small channel spacing combined with a broadband functionality are well sought after. Over the past years a range of plasmonic wavelength demultiplexers (WDs) have been proposed [9–12,15,16,18] and experimentally developed [3,17,19]. However, to our knowledge, only a few plasmonic WDs have been experimentally characterized in the near-infrared communication regime, and those offer a relatively large channel spacing, viz., larger than 100 nm [17]. At the same time, beam splitters and wavelength filters are elements universally used in photonic integrated circuits [20,21], while components with an adaptable functionality, such as the recently demonstrated all-in-one light alignment controllable beam splitter [20,21], can be useful for optical on-chip reconfigurable circuits [22]. Furthermore, it has been recently demonstrated [23] that inherently lossy controllable plasmonic beam splitters [20,21] could be used in the decomposition and implementation of general linear transformations in photonic circuits platforms [23] as well as to realize a quantum random number generator [24] or to conduct the plasmonic version of the Hong–Ou–Mandel (HOM) experiment [25,26].

In this work, we experimentally demonstrate the capability of a simple, microscale, planar, and easily fabricated plasmonic structure—based on a periodically perforated gold (Au) plasmonic metasurface (PM) attached on a glass substrate—to nondestructively sample a propagating light beam and perform five functionalities in the signal sample; two of these processes have already been demonstrated [8,14,27], and three of them are herein demonstrated for the first time to our knowledge. We do not focus on the already experimentally demonstrated [8,14,27] (a) light-to-surface plasmon conversion and (b) polarization

measurement and four-level polarization demultiplexing. Those works [8,14,27] demonstrated demultiplexing for signals linearly polarized with azimuthal angles $\theta = 0°, 45°, 90°, 135°$ and at *a wavelength within a 7 nm "colorless" wavelength range* [8], over which the maximum coupling efficiencies to the surface plasmon polariton (SPP) eigenmodes excited at the air–Au and glass–Au interfaces (achieved when the illuminating beam polarization is aligned with the eigenmode orientation) were virtually identical (less than 1% difference). Rather, we here focus on the functionalities that the structure performs outside the aforementioned "colorless" wavelength range [8], i.e., in the wavelength ranges where the coupling efficiencies to the SPP eigenmodes excited at the air–Au and glass–Au interfaces, for input polarization aligned to the eigenmode orientation, are not equal but depend on the wavelength of the input signal. Our device can be used for two-channel wavelength demultiplexing, i.e., separation of signals with *the same polarization but different wavelengths*, offering, to our knowledge, the smallest channel spacing (43.7 nm) experimentally demonstrated for a plasmonic structure in the near-infrared communication regime. For comparison, as mentioned above, the channel spacing offered by conventional plasmonic components (experimentally demonstrated at that regime) is usually larger than 100 nm. Second, it can perform wavelength *and* polarization controllable beam splitting of a *monochromatic, single polarization* signal, over a wavelength range of at least 77 nm. The structure splits the signal in two or four primary prongs, along with four or two prongs of lesser (2.8–3.9 times less) power, respectively. The number of primary prongs in which the signal sample splits, along with their power ratio and orientation, can be controlled by the wavelength *and* the polarization of the input light beam. To our knowledge, this is the first time that a plasmonic beam splitter has been experimentally demonstrated to divide a *monochromatic, single polarization* signal to a prong number dictated by the signal wavelength-polarization combination. Third, the device is capable of demultiplexing four wavelength-polarization conditions and routing them toward uniquely connected bidirectional orientations, thereby enabling quadruple the data density of an interconnect (when combined with a wavelength-polarization multiplexing scheme). The favorable combination of microscale footprint [28], relatively broadband functionality [29], and relatively small channel spacing [30] makes the structure suitable for both sensing and on-chip communication applications. Moreover, the characteristic feature of the metasurface [31–33] to enable high direct transmission while (for the wavelength range considered here) maintaining the properties of the input (directly transmitted) beam, allows for in-line nondestructive sensing and parallel signal processing [21].

2. SAMPLES AND EXPERIMENTAL ARRANGEMENT

A scanning microscopy image (SEM) of the PM structure used in this work is shown in Fig. 1(a). It was fabricated by focused ion beam (FIB) milling in a magnetron-sputtered deep-subwavelength 50 nm thick Au film attached on a 700 μm glass substrate [6,8,14,27]. The substrate thickness can in principle become much thinner if, e.g., it is made of a different material with a similar refractive index. It was circular, with a 40 μm diameter, and consisted of deep-subwavelength 300 nm diameter circular holes, periodically perforated in a 1530 nm period square lattice [6,8,14,27]. Although the herein presented structure had a 40 μm diameter, the size could be scaled down to a 30.6 μm diameter (∼441 holes) without changing their functionality [34]. The PM structure was surrounded by a 120 μm internal diameter and 1.5 μm width circular slit as shown in the SEM image [Fig. 1(b)] and in the not-to-scale schematic [Fig. 1(c)], which allowed the SPP signal launching from the PM onto the surrounding smooth metal film to be detected in the far field, after scattering into photons [6,8,14,27]. The PM transmission dispersion, shown in Fig. 1(e), was investigated by measuring the zero-order far-field transmission spectra of the structure for different angles of incidence γ, under illumination with x-polarized light, as described in [6,35].

A periodically perforated plasmonic metasurface with a square lattice supports several SPP Bloch modes that are the eigenmodes of the structure [35], and it can be theoretically approximated using a perturbative approach, valid in the limit of infinitely small holes and away from the areas where the eigenmodes tend to cross and thus bandgaps are formed [35,36], according to which the dispersion relation of the SPP Bloch modes can be written as the folding of the dispersion relation of the flat interface SPP [Eq. (1)]:

$$k_{\mathrm{BSPP}} = k_{\mathrm{SPP}} + \frac{2\pi}{D}\left(p\vec{u}_x + q\vec{u}_y\right), \tag{1}$$

where k_{BSPP} and $k_{\mathrm{SPP}}(=\frac{2\pi}{\lambda}\sqrt{\frac{\varepsilon_m\varepsilon_d}{\varepsilon_m+\varepsilon_d}})$ are the wave vectors of the SPP Bloch modes on the periodically perforated plasmonic metasurface and the SPPs on a smooth surface, respectively; D is the lattice period; u_x and u_y are the unit vectors of the reciprocal lattice; p and q are integers related to the several diffraction modes; λ is the illuminating light wavelength; and ε_m, ε_d are the dielectric constants of the metal and dielectric materials, respectively. This first approximation ignores the effect of the hole geometric properties, namely, shape and size, at the SPP dispersion as well as the SPP coupling, which is particularly strong close to the bandgap areas, such as the one located at the Brillouin zone center, where the Bloch modes tend to cross [35]. The eigenmodes of the structure can be identified in the PM transmission dispersion [Fig. 1(e)] since they are responsible for the transmission enhancement [35]. The solid lines show the analytically approximated, using Eq. (1), eigenmodes for the air–Au interfaces (green lines, denoted with the subscript "a") and the glass–Au (pink lines, denoted with the subscript "g") interfaces. Although Eq. (1) is only a first-order approximation, the analytically approximated eigenmodes are in relatively good agreement with the experimental ones at the areas away from the bandgaps. The PM has been designed such that the $(\pm1, 0)_a$ and $(0, \pm1)_a$ SPP Bloch modes of the air–Au interface are spectrally situated close to the $(-1, \pm1)_g$ modes of the glass–Au interface, at the vicinity of the Brillouin zone center [6,8,14,27]. The $(0, \pm1)_a$ eigenmodes replace the $(\pm1, 0)_a$ ones under vertically polarized illumination

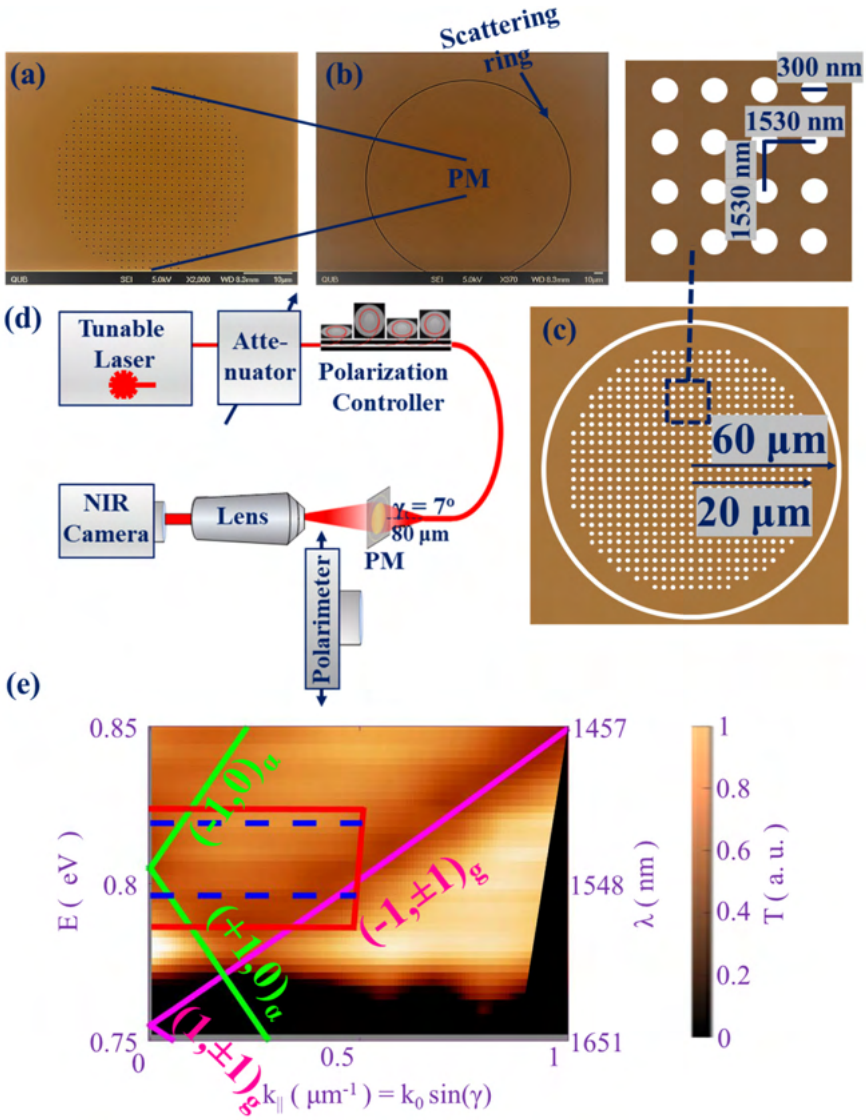

Fig. 1. (a) SEM image of the PM structure, (b) SEM image, and (c) schematic (not in scale) of the PM structure and the surrounding scattering ring. (d) Experimental arrangement for investigating the in-plane SPP signal transmission around the PM structure. (e) Measured PM transmission dispersion (2D map) and the estimated eigenmode positions using Eq. (1) (solid lines) for horizontally polarized illumination. The estimated air–Au eigenmodes are shown in green and denoted by "a," while the glass–Au ones are shown in pink and have been marked with the subscript "g." The red box indicates the spectral area excited when the PM is illuminated with horizontally polarized light at the wavelength range 1502–1577 nm. The corresponding spectral areas for $\lambda = 1511.3$ nm and $\lambda = 1555$ nm are denoted with blue dashed lines. The black areas are spectral areas that are not covered with experimental data.

[6,8,14,27]. The wavelength and polarization-dependent in-plane SPP signal transmission angular distribution around the PM structure was experimentally investigated using the experimental arrangement shown in Fig. 1(d). The PM structure was illuminated with a polarized laser beam through an antireflection-coated single-mode patch cord, coupled to a polarization controller and a tunable infrared laser, operating at the S and C telecom bands (1502–1577 nm). The patch cord numerical aperture was 0.13, and thus the PM structure was illuminated in the range of 0°–7° angles of incidence [8]. An attenuator was used between the laser and the polarization controller to allow the laser to work at an optimum output power but protect the sensitive infrared camera from damage due to overexposure.

3. RESULTS AND DISCUSSION

Figure 2 shows the far-field SPP intensity distributions on the PM and surrounding scattering ring, when the structure is illuminated with a 7° divergent laser beam linearly polarized at azimuthal angles $\theta = 0°, 90°, 45°$, and 135°, at the wavelengths $\lambda_1 = 1511.3$ nm and $\lambda_2 = 1555$ nm, using the experimental arrangement shown in Fig. 1(d). The corresponding excited spectral areas, for $\theta = 0°$, have been marked with blue dashed lines at Fig. 1(e). The central area is the image of the PM itself, and it is saturated due to the high (∼ 25%) direct, undisturbed (the beam preserves all its properties, besides power) transmission through the nanostructured area [8,14,21,32,33]. The divergent nature of the illumination beam allows for the

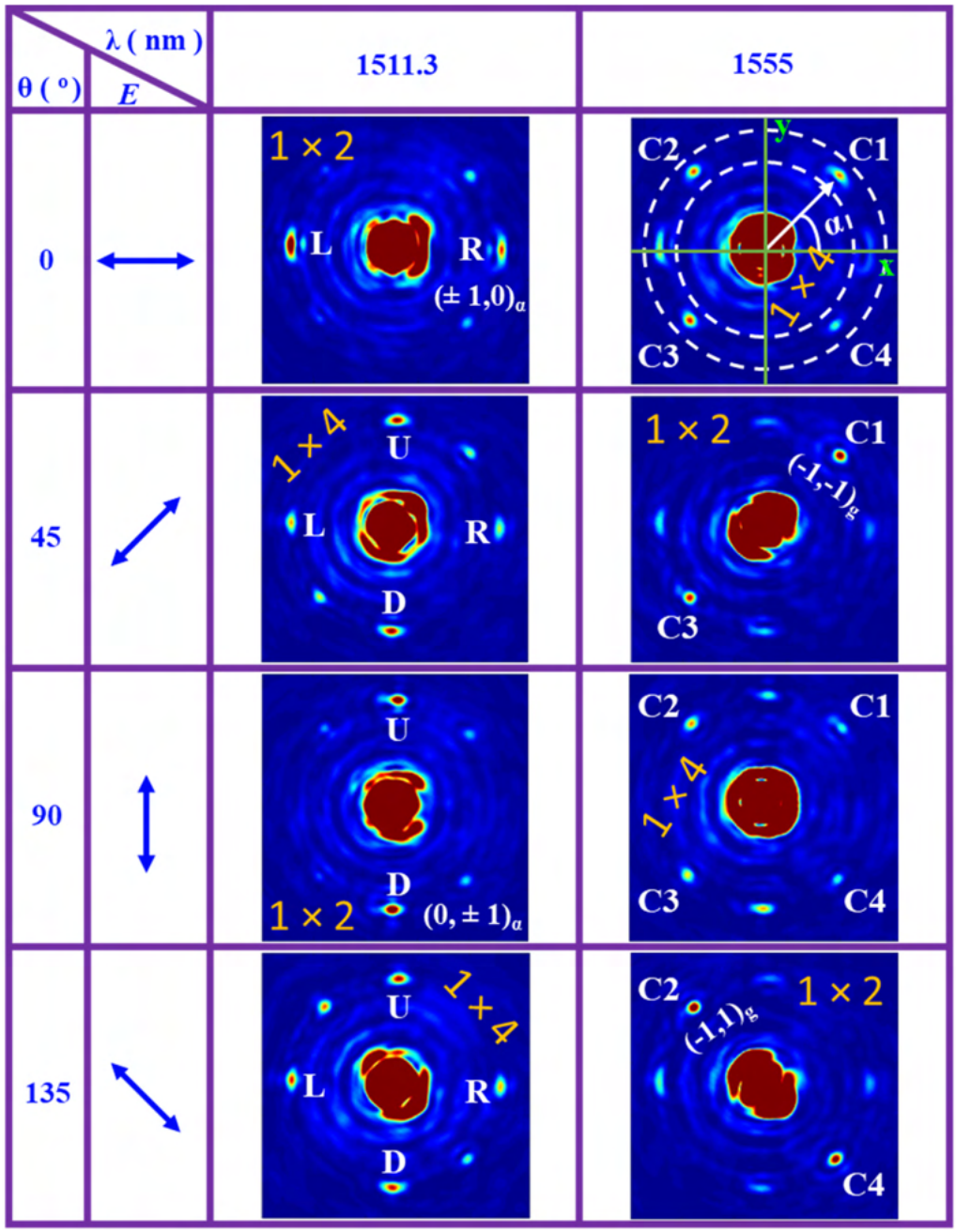

Fig. 2. Far-field images of the scattered light intensity (corresponding to SPP intensity) on and around the PMs surrounded by the scattering ring, when these are illuminated with a monochromatic ($\lambda = 1511.3$ nm or $\lambda = 1555$ nm) linearly polarized illumination with azimuthal angles $\theta = 0°$, 90°, 45°, or 135° laser beam, out of a single-mode fiber (NA: 0.13). The beam-splitting functionality and the primary output prongs ({U, D, R, L, C1, C2, C3, C4}) are shown for each wavelength-polarization combination. The air–Au and glass–Au eigenmodes are denoted by the subscripts "a" and "g," respectively. The angle α and the annular aperture (white dashed circles) encompassing the scattering ring, to which we refer in the text, are also shown.

simultaneous excitation of the eigenmodes at the two interfaces (air–Au and glass–Au), while the scattering ring cutting through the Au film enables their concurrent detection. The light intensity SPP waves observed at the output ports (spatially separated angles α) R (−2.3°), C1 (43.3°), U (88.3°), and C2 (133.9°) correspond to the SPP eigenmodes $(\pm 1, 0)_a$, $(-1, -1)_g$, $(0, \pm 1)_a$, and $(-1, +1)_g$, where "a" and "g" denote the SPP eigenmodes excited at the air–Au and glass–Au interfaces, respectively; light intensity corresponding to the same SPP eigenmodes is observed in the counterpart hemisphere (L, C3, D, C4). For the wavelengths considered here, the SPP fields do not penetrate the metal film to a sufficient depth to lead to (significant) coupling between the SPPs propagating at the two interfaces; the penetration depth δ_m is ∼ 24 nm as calculated by the expression $\delta_m = \frac{1}{k_0}\left|\frac{\varepsilon'_m+\varepsilon_d}{\varepsilon'^2_m}\right|$ [37], where k_0 is the free-space wavenumber, ε'_m is the real part of the dielectric

constant of the metal (Au), and ε_d is the dielectric constant of the dielectric material (air or glass). The observed SPP waves are launched by the PM on the surrounding smooth Au film and observed into the far field after being converted into photons by the scattering ring. The SPP power detected at the output ports around the PM depends on the wavelength and the polarization of the illuminating laser beam [8]. The polarization dependence is dictated by the inherent SPP transverse magnetic nature [8,14,35]. The wavelength dependence is a combination of the wavelength-dependent coupling efficiency to the several excited eigenmodes and the propagation of the eigenmodes on interfaces (air–Au and glass–Au) with unequal refractive indices experiencing unequal losses [8].

The functionality of the PM structure was investigated at the wavelength range 1502–1577 nm, for linear polarizations with azimuthal angles $\theta = 0°$, 45°, 90°, and 135°, under the 7° divergent illumination. The corresponding excited spectral area for the case of the horizontal illumination ($\theta = 0°$) is marked with a red box in Fig. 1(e). For each polarization state, the wavelength range was scanned with a 0.1 nm resolution, and the far-field light intensity distribution corresponding to the SPP intensity distribution on the PM and the surrounding scattering ring was imaged on the infrared camera for each value of the illuminating wavelength. The illuminating light polarization was checked regularly, every 1 nm, with a polarimeter, which was mounted on a translation stage, such as to go in and out the experimental arrangement as shown in Fig. 1(d), and, if needed, the polarization of the illuminating beam was readjusted to stay at the desired polarization state using the polarization controller. Since the properties of the illuminating beam do not alter transmission through the PM structure (at the wavelengths under consideration), the polarization was measured after the PM structure per convenience. The captured images were first transformed into polar coordinates, and then the light intensity was integrated over an annular aperture that encompasses the scattering ring as shown in Fig. 2 and over angular sections of 0.7°, corresponding to the camera pixels. The SPP signal transmission for an illuminating wavelength value λ, at the angular in-plane position α of the scattering ring, was calculated as the ratio of the scattered light power from that angular position [as detected on the charge-coupled (CCD) camera] over the power (detected on the CCD camera) in the absence of the sample, for the same wavelength and polarization.

Figures 3(a)–3(d) show the SPP transmission as a function of the illuminating wavelength λ and the angular position α (as defined in Fig. 2) for the cases of linearly polarized illumination with azimuthal angles $\theta = 0°$, 45°, 90°, 135° (after mathematically filtering out the substrate and the fiber-sample Fabry–Perot cavity ripples [21]). When the PM structure is illuminated with a *monochromatic*, *single polarization* input beam, the in-plane signal splits into two or four primary prongs, along with four or two additional prongs of lesser (2.8–3.9 times less) power, respectively. The number of primary prongs, their relative power, and their orientation are controlled by the wavelength and the polarization of the signal, rendering a wavelength-polarization controllable beam splitting functionality. Figures 2 and 3(a)–3(d) show the primary prongs for each wavelength–polarization combination. The coupling efficiency to the horizontally or vertically $[(\pm 1, 0)_a$ or $(0, \pm 1)_a]$ and diagonally $(-1, \pm 1)_g$ propagating eigenmodes is maximized around $\lambda_1 = 1511.3$ nm and $\lambda_2 = 1555$ nm, respectively. The input polarization is analyzed in the orientations of the "maximized" eigenmodes, i.e., the eigenmodes with the highest coupling efficiency in the illumination wavelength, resulting in either a 1×2 or 1×4 beam splitting. For horizontal and vertical polarization and free-space wavelength around $\lambda_2 = 1555$ nm, the in-plane signal sample splits into four primary prongs routed toward C1, C2, C3, and C4. On the contrary, it splits into two primary prongs routed toward R, L (for horizontal polarization) or toward U, D (for vertical polarization), if the illuminating free-space wavelength is around $\lambda_1 = 1511.3$ nm. Similarly, for linear polarization with azimuthal angle $\theta = +45°$ or $+135°$, the in-plane signal splits into four primary prongs, routed toward U, D, R, L if the illuminating wavelength is around 1511.3, and into two primary prongs, routed toward C1, C3 for $\theta = +45°$ or C2, C4 for $\theta = 135°$, if the illuminating wavelength is around 1555 nm. The beam splitter operates for a wavelength range of at least 75 nm (1502–1577 nm), providing a 3 dB bandwidth of at least 37 nm ($W_1 = 1502-1539$ nm) around 1511.3 nm and at least 50 nm ($W_2 = 1527-1577$ nm) around 1555 nm. The examined wavelength range was limited by the wavelength range over which the tunable laser can be tuned. For an ideal alignment (and the considered polarization states), the power at the primary prongs is identical (for each of the wavelength-polarization combinations). Any power differences observed at Figs. 2 and 3 among the prongs of the beam splitter (for a given wavelength-polarization combination) are due to a small misalignment between the PM and the illumination beam centers and a small tilt between the out-of-plane illumination beam z axis and the normal to the PM.

Furthermore, the capability of the PM to route signals of two different wavelength ranges in different orientations allows the structure to function as a wavelength demultiplexer in a plasmonic or photonic communication link, enabling the doubling of its information capacity. By taking vertical cross sections from Fig. 3(a), the transmission spectra of the output ports R and C2, when the illumination polarization is horizontal, have been plotted in Fig. 3(f). The signals of two wavelength multiplexed channels with central wavelengths $\lambda_1 = 1511.3$ nm and $\lambda_2 = 1555$ nm are demultiplexed and routed toward R and $C2$, respectively, where they are detected with a −4.5 dB–−5.9 dB crosstalk. The power detected at the output ports is stable (varies less than 1%) over a 19 nm wavelength span around the two central wavelengths, viz., 1505–1524 nm and 1545–1564 nm. The relatively high crosstalk could be reduced by either eliminating the "unwanted" signal, or by enhancing the coupling to the "desired" mode. One way to practically reduce the detection of the "unwanted" signal while maintaining the high direct transmission of the illuminating beam is to embed a threshold mechanism at the in-plane output ports [4]. Alternatively, the coupling to the "desired" in-plane mode can be enhanced by employing critical coupling [38–40]. To achieve this, a multilayer dielectric Bragg mirror could be placed at the rear surface of the glass substrate [40], and the dissipation losses of the sample and the input signal would need to be engineered

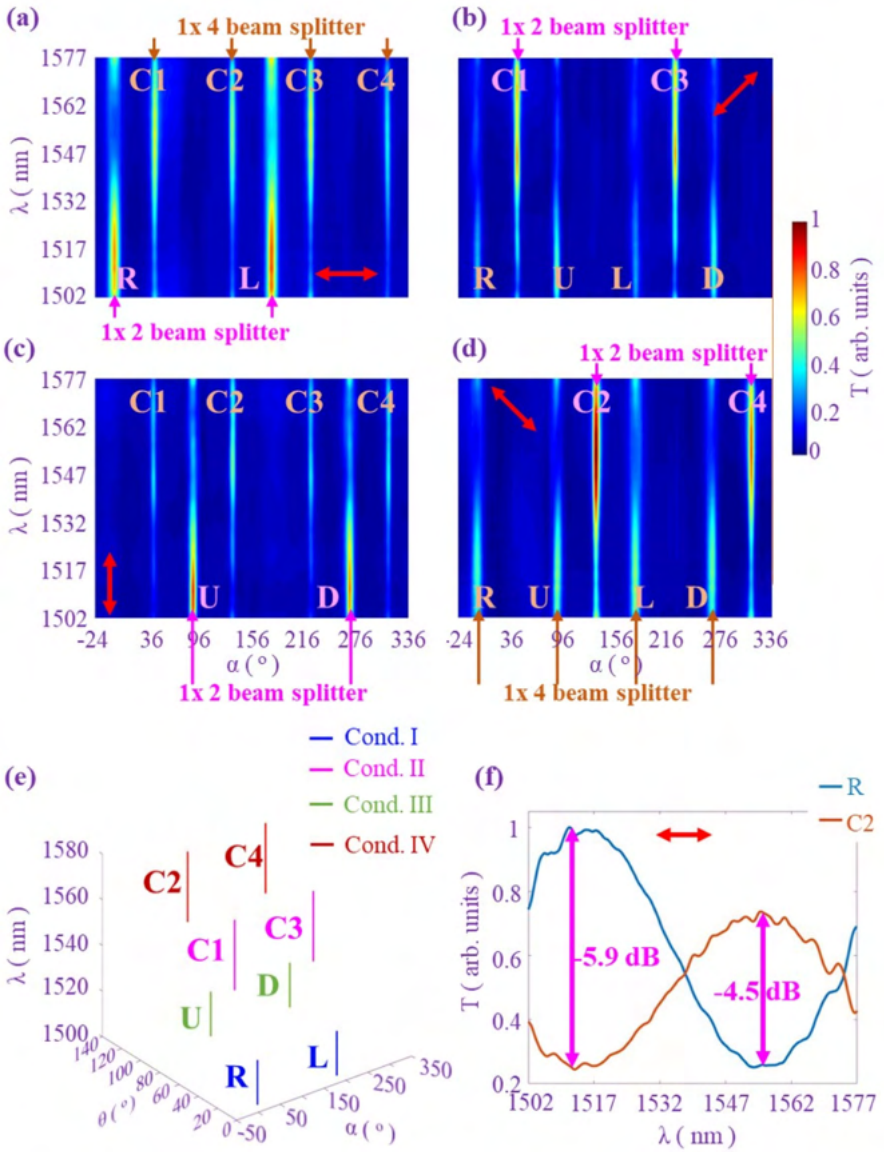

Fig. 3. (a)–(d) Normalized angular distribution of the SPP signal transmission spectra at the scattering ring surrounding the PM for linearly polarized illumination at azimuth angles θ (a) 0° (horizontal), (b) 45°, (c) 90° (vertical), and (d) 135°, after mathematically filtering out the fine ripples due to the fiber sample and substrate cavities. The angular positions of the primary prongs have been marked at the graphs. (e) The uniquely demultiplexed logic states 1 as a function of the angular in-plane angular position α, the azimuthal angle θ, and the illuminating wavelength λ. (f) The normalized SPP transmission spectra at the output ports R and C2, for a horizontal illumination. The illuminating electric field projection on the PM plane is denoted in each graph with a red arrow.

such that the absorption rate of the "desired" mode (at the wavelength of interest) in the sample to become equal to the leakage (reflection) rate of that mode out of (from) the sample [38–40]. Implementing critical coupling would also lead to maximizing the coupling efficiency to the in-plane signal while at the same time eliminating the direct transmission of the illuminating beam [38–40].

In addition, similarly to Ref. [4], the PM structure can be used to demultiplex four wavelength-polarization conditions, enabling, when combined with a wavelength-polarization multiplexing scheme, the quadruple of a communication link throughput. By setting the transmission above 0.62 a.u at the four angular positions R, C1, U, C2 and their counterparts, L, C3, D, C4, as the logic state "1" or "ON" state and the transmission below that value as the logic state "0" or "OFF," then the output of the four channel pairs can be switched between the ON and OFF states according to the incident wavelength and polarization. Table 1 illustrates the response results of the channel pairs at four different wavelength-polarization conditions, and Fig. 3(e) graphically presents the four conditions that switch ON the four channel pairs. It is evident that the ON state of the four channel pairs is uniquely connected with one and only condition, demonstrating in this way the wavelength-polarization demultiplexing and routing functionality of the structure.

Table 1. Channel Response to the Four Wavelength-Polarization Multiplexed Conditions

Input			Output			
			Channel Pair			
Condition	Polarization θ (°)	Wavelength Range λ (nm)	$R-L$	$C1-C3$	$U-D$	$C2-C4$
I	0	1503.5–1523.1	1	0	0	0
II	45	1538.6–1569.4	0	1	0	0
III	90	1503.5–1523.1	0	0	1	0
IV	135	1538.6–1569.4	0	0	0	1

4. CONCLUSION AND OUTLOOK

In conclusion, we have experimentally demonstrated that a simple, easily fabricated, microscale PM structure can sample a light beam, without altering its properties, and perform five functionalities on the signal sample. The structure, on top of the already demonstrated [8,14,27] light-to-surface-plasmon coupling, and polarization measurement and four-level polarization demultiplexing of signals with the *same wavelength*, within a 7 nm "colorless" wavelength span [8], it is herein demonstrated to perform the three functionalities outlined below. The device can operate as a broadband wavelength-polarization controllable beam splitter of a *monochromatic, single polarization* signal. The number, orientation, and relative power of the prongs that the signal will be divided into is controlled by the wavelength and polarization of the signal. Second, it enables two-channel wavelength demultiplexing, providing a small channel spacing (43.7 nm) and power stability (less than 1% variation) at the output ports over a 19 nm span around their central wavelengths. Third, the structure can function as a four-level wavelength-polarization demultiplexer, enabling the quadruplication of information density of a communication link (when combined with a wavelength-polarization multiplexing scheme).

While the SPP signal power in our experiment is measured off-plane after converting to photons, one could envision the integration of the plasmonic metasurfaces with in-plane detectors [41] or in-plane output dielectric waveguides [42,43] (coupling the signal from both air–Au and glass–Au interfaces), enabling a completely standalone device. Moreover, the device could be used as part of an all-planar circuit [3] at which the input signal would also be transmitted by a planar dielectric waveguide [42,43] instead of impinging from free space. In this scenario, the coupling to the PM is expected to improve compared the in-coupling from free space. For the structure to retain the same functionalities, the input illumination needs to be designed to cover the same spectral area and couple in both air–Au and glass–Au interfaces of the structure. Furthermore, mechanisms such as threshold or critical coupling to the individual modes [40] could be employed to optimize the structure performance, including reducing the crosstalk of wavelength demultiplexing. Achieving (close to) critical coupling would also eliminate the out-of-plane signal and maximize the in-plane coupling efficiency [38–40]. Even though the structure was designed to operate in the S and C telecom wavelength bands, the operating wavelength can be tuned across the whole range, from ultraviolet to infrared by changing the PM lattice period [32]. The fabrication ease and the versatile, all-in-one nature of the device, combined with its capability to offer undisturbed in-line sampling of the input signal, could make it an essential element of adaptable integrated photonic circuits used in a variety of applications including enhanced bandwidth on-chip communications, parallel computing, and nondestructive sensing.

Funding. Hellenic Foundation for Research and Innovation (1819); General Secretariat for Research and Technology (1819); Engineering and Physical Sciences Research Council.

Acknowledgment. We thank the Photonics and Nanotechnology group, Department of Physics, King's College London, UK, for providing the samples and SEM images, as well as the Optical Networks Group, Department of Electronic & Electrical Engineering, University College London, UK, for therein performing the reported measurements as part of M. I. B.'s PhD research. M. I. B. acknowledges EPSRC, UK, for a PhD scholarship funding. K. L. T. was supported by the General Secretariat for Research and Technology (GSRT) and the Hellenic Foundation for Research and Innovation (HFRI), Greece, under Grant No. 1819.

Disclosures. The authors declare no conflicts of interest.

Data Availability. Data underlying the results presented in this paper are not publicly available at this time but may be obtained from the authors upon reasonable request.

REFERENCES

1. M. L. Brongersma and V. M. Shalaev, "The case for plasmonics," Science **328**, 440 (2010).
2. K. L. Tsakmakidis and O. Hess, "Extreme control of light in metamaterials: complete and loss-free stopping of light," Physica B **407**, 4066–4069 (2012).
3. L. Li, T. Li, S. Wang, S. Zhu, and X. Zhang, "Broad band focusing and demultiplexing of in-plane propagating surface plasmons," Nano Lett. **11**, 4357–4361 (2011).
4. J. Ji, Y. Zhai, Z. Wu, X. Ma, and Q. Wang, "Wavelength-polarization multiplexer for routing and detection of surface plasmon polaritons based on plasmonic gratings," ACS Photon. **7**, 2115–2121 (2020).
5. M. I. Benetou, W. Dickson, V. Mikhailov, B. Thomsen, P. Bayvel, and A. V. Zayats, "Dispersive properties of surface plasmon polaritonic crystals with different boundary shapes," *IEEE Leos Annual Meeting Conference Proceedings*, Belek-Antalya, Turkey (2009), pp. 100–101.
6. M. I. Benetou, *Surface Plasmon Polaritonic Crystals for Applications in Optical Communications* (University College London, 2019).
7. M. I. Benetou, J.-S. Bouillard, P. Segovia, W. Dickson, B. C. Thomsen, P. Bayvel, and A. V. Zayats, "Boundary effects in finite size plasmonic crystals: focusing and routing of plasmonic beams for optical communications," Nanotechnology **26**, 444001 (2015).
8. M. I. Benetou, B. Thomsen, P. Bayvel, W. Dickson, and A. Zayats, "Four-level polarization discriminator based on a surface plasmon polaritonic crystal," Appl. Phys. Lett. **98**, 111109 (2011).
9. Y.-D. Wu, "High transmission efficiency wavelength division multiplexer based on metal–insulator–metal plasmonic waveguides," J. Lightwave Technol. **32**, 4844–4848 (2014).

10. R. Guo, M. Decker, I. Staude, D. N. Neshev, and Y. S. Kivshar, "Bidirectional waveguide coupling with plasmonic Fano nanoantennas," Appl. Phys. Lett. **105**, 053114 (2014).
11. Y.-Y. Xie, C. He, J.-C. Li, T.-T. Song, Z.-D. Zhang, and Q.-R. Mao, "Theoretical investigation of a plasmonic demultiplexer in MIM waveguide crossing with multiple side-coupled hexagonal resonators," IEEE Photon. J. **8**, 4802512 (2016).
12. G. Wang, H. Lu, X. Liu, D. Mao, and L. Duan, "Tunable multi-channel wavelength demultiplexer based on MIM plasmonic nanodisk resonators at telecommunication regime," Opt. Express **19**, 3513–3518 (2011).
13. A. G. Joly, Y. Gong, P. Z. El-Khoury, and W. P. Hess, "Surface plasmon-based pulse splitter and polarization multiplexer," J. Phys. Chem. Lett. **9**, 6164–6168 (2018).
14. M. I. Benetou, B. C. Thomsen, W. Dickson, P. Bayvel, and A. V. Zayats, "Surface plasmon polaritonic crystal polarisation demultiplexer for 4 level polarisation-shift-keying," in *The UK's Premier Conference in Optics and Photonics (Photon 10)*, Southampton, UK (2010), p. 106.
15. A. Udupi and S. K. Madhava, "Plasmonic coupler and multiplexer/demultiplexer based on nano-groove-arrays," Plasmonics (to be published).
16. U. Aparna, H. S. Mruthyunjaya, and M. S. Kumar, "Plasmonic nanoslit-based dual-wavelength multiplexer," J. Opt. **49**, 17–22 (2020).
17. R. Guo, M. Decker, F. Setzpfandt, I. Staude, D. N. Neshev, and Y. S. Kivshar, "Plasmonic Fano nanoantennas for on-chip separation of wavelength-encoded optical signals," Nano Lett. **15**, 3324–3328 (2015).
18. Q. Gan, B. Guo, G. Song, L. Chen, Z. Fu, Y. J. Ding, and F. J. Bartoli, "Plasmonic surface-wave splitter," Appl. Phys. Lett. **90**, 161130 (2007).
19. Z. Liu, X. Liu, Z. Xiao, C. Lu, H.-Q. Wang, Y. Wu, X. Hu, Y.-C. Liu, H. Zhang, and X. Zhang, "Integrated nanophotonic wavelength router based on an intelligent algorithm," Optica **6**, 1367–1373 (2019).
20. M. I. Benetou, "SPPC based beam splitter and alignment sensor: the passive and active control of its functionality parameters," in *Frontiers in Optics + Laser Science APS/DLS*, Washington, D. C. (Optical Society of America, 2019), paper JW3A.68.
21. M. I. Benetou and K. L. Tsakmakidis, "Light-alignment controllable beam splitter and vectorial displacement sensor in the stopped-light regime of plasmonic metasurfaces," ACS Photon. **8**, 296–306 (2021).
22. M. Papaioannou, E. Plum, J. Valente, E. T. F. Rogers, and N. I. Zheludev, "Two-dimensional control of light with light on metasurfaces," Light Sci. Appl. **5**, e16070 (2016).
23. S. Kasture, "Designing optical circuits using plasmonic beam splitters," Opt. Lett. **43**, 2547–2550 (2018).
24. J. T. Francis, X. Zhang, Ş. K. Özdemir, and M. Tame, "Quantum random number generation using an on-chip plasmonic beamsplitter," Quantum Sci. Technol. **2**, 035004 (2017).
25. G. Di Martino, Y. Sonnefraud, M. S. Tame, S. Kéna-Cohen, F. Dieleman, Ş. K. Özdemir, M. S. Kim, and S. A. Maier, "Observation of quantum interference in the plasmonic Hong-Ou-Mandel effect," Phys. Rev. Appl. **1**, 034004 (2014).
26. B. Vest, M.-C. Dheur, É. Devaux, A. Baron, E. Rousseau, J.-P. Hugonin, J.-J. Greffet, G. Messin, and F. Marquier, "Anti-coalescence of bosons on a lossy beam splitter," Science **356**, 1373 (2017).
27. M. I. Benetou, W. Dickson, B. C. Thomsen, P. Bayvel, and A. V. Zayats, "Microscale polarimeter based on a plasmonic crystal," in *The 5th International Conference on Surface Plasmon Photonics Conference Proceedings (SPP5)*, Busan, South Korea (2011), p. 135.
28. F. Y. Gardes, K. L. Tsakmakidis, D. Thomson, G. T. Reed, G. Z. Mashanovich, O. Hess, and D. Avitabile, "Micrometer size polarisation independent depletion-type photonic modulator in silicon on insulator," Opt. Express **15**, 5879–5884 (2007).
29. K. L. Tsakmakidis, O. Reshef, E. Almpanis, G. P. Zouros, E. Mohammadi, D. Saadat, F. Sohrabi, N. Fahimi-Kashani, D. Etezadi, R. W. Boyd, and H. Altug, "Ultrabroadband 3D invisibility with fast-light cloaks," Nat. Commun. **10**, 4859 (2019).
30. L. Su, A. Y. Piggott, N. V. Sapra, J. Petykiewicz, and J. Vučković, "Inverse design and demonstration of a compact on-chip narrowband three-channel wavelength demultiplexer," ACS Photon. **5**, 301–305 (2018).
31. T. W. Ebbesen, H. J. Lezec, H. F. Ghaemi, T. Thio, and P. A. Wolff, "Extraordinary optical transmission through sub-wavelength hole arrays," Nature **391**, 667–669 (1998).
32. C. Genet and T. W. Ebbesen, "Light in tiny holes," Nature **445**, 39–46 (2007).
33. M. I. Benetou, J.-S. Bouillard, W. Dickson, B. C. Thomsen, P. Bayvel, and A. V. Zayats, "Visualization of high-order plasmonic Bloch modes in square-lattice plasmonic crystal," in *The 5th International Conference on Surface Plasmon Photonics Conference Proceedings (SPP5)*, Busan, South Korea (2011), p. 237.
34. F. J. Garcia-Vidal, L. Martin-Moreno, T. W. Ebbesen, and L. Kuipers, "Light passing through subwavelength apertures," Rev. Mod. Phys. **82**, 729–787 (2010).
35. H. F. Ghaemi, T. Thio, D. E. Grupp, T. W. Ebbesen, and H. J. Lezec, "Surface plasmons enhance optical transmission through subwavelength holes," Phys. Rev. B **58**, 6779–6782 (1998).
36. C. Billaudeau, S. Collin, C. Sauvan, N. Bardou, F. Pardo, and J.-L. Pelouard, "Angle-resolved transmission measurements through anisotropic two-dimensional plasmonic crystals," Opt. Lett. **33**, 165–167 (2008).
37. W. L. Barnes, "Surface plasmon–polariton length scales: a route to sub-wavelength optics," J. Opt. A **8**, S87–S93 (2006).
38. Z. Fang, Y.-R. Zhen, L. Fan, X. Zhu, and P. Nordlander, "Tunable wide-angle plasmonic perfect absorber at visible frequencies," Phys. Rev. B **85**, 245401 (2012).
39. D. G. Baranov, A. Krasnok, T. Shegai, A. Alù, and Y. Chong, "Coherent perfect absorbers: linear control of light with light," Nat. Rev. Mater. **2**, 17064 (2017).
40. J. R. Piper and S. Fan, "Total absorption in a graphene monolayer in the optical regime by critical coupling with a photonic crystal guided resonance," ACS Photon. **1**, 347–353 (2014).
41. P. Berini, "Surface plasmon photodetectors and their applications," Laser Photon. Rev. **8**, 197–220 (2014).
42. M. Hochberg, T. Baehr-Jones, C. Walker, and A. Scherer, "Integrated plasmon and dielectric waveguides," Opt. Express **12**, 5481–5486 (2004).
43. O. Tsilipakos, A. Pitilakis, T. V. Yioultsis, S. Papaioannou, K. Vyrsokinos, D. Kalavrouziotis, G. Giannoulis, D. Apostolopoulos, H. Avramopoulos, T. Tekin, M. Baus, M. Karl, K. Hassan, J.-C. Weeber, L. Markey, A. Dereux, A. Kumar, S. I. Bozhevolnyi, N. Pleros, and E. E. Kriezis, "Interfacing dielectric-loaded plasmonic and silicon photonic waveguides: theoretical analysis and experimental demonstration," IEEE J. Quantum Electron. **48**, 678–687 (2012).